Radio variability in the young stellar cluster Ophiuchus A

Author: Arnau Vicente Bou, avicenbo74@alumnes.ub.edu
Facultat de Física, Universitat de Barcelona, Diagonal 645, 08028 Barcelona, Spain.

Advisor: Gemma Busquet Rico, gbusquet@fqa.ub.edu

Abstract: Utilizing VLA X-band ($\sim$ 10 GHz) observations of the Ophiuchus A young stellar cluster, we study the flux variability of the sources in that region for 17 different epochs spanning approximately one month. In the first part of this work we perform an iterative self-calibration procedure of the visibilities to correct phase and amplitude artifacts, generating 2-field mosaics for each epoch. In the second part, we extract de fluxes of the 22 objects detected across all epochs and establish a variability classification scheme based on comparing each source's maximum flux difference to a threshold that takes into account both rms and calibration uncertainties. Our results reveal variability in 15 out of the 22 detected sources, with particularly notable cases such as pronounced emission peaks in GGS29 and GGS30-IRS2, as well as a variable flux from the VLA1623A binary system. Furthermore, the sample studied seems to be consistent with the idea that Young Stellar Objects' (YSOs) variability increases with their evolutionary stage.
Keywords: star formation, molecular cloud, accretion disc, thermal emission, flux variability.
SDGs: quality education; industry, innovation, infrastructure; alliance for objectives.

I. INTRODUCTION

Interstellar molecular clouds hold significant scientific interest as they allow for a complete monitoring of the early stages of star formation. The protostellar bodies embedded in these regions are referred to as Young Stellar Objects (YSOs) and are surrounded by a rotating and accreting envelope of gas and dust that over time evolves into a protostellar disc. This project will focus on characterizing the flux variability of these YSOs, which spans widely diverse timescales ranging from either few seconds to days when linked to non-thermal phenomena such as magnetospheric instabilities (mostly in Class II/III pre-main sequence stars), to months or even decades when derived from thermal processes (in Class 0/I); as stated in [1] and [2].

For this analysis, we rely on several observations carried out with the Karl G. Jansky Very Large Array (VLA) in its most extended antenna configuration (A-array, with a maximum baseline of 36.4 km) specifically in the X-band (i.e. 8-12 GHz or 3.6 cm wavelength), that are part of a larger project proposal [3]. This frequency band traces thermal emission from ionized gas (free-free) resulting from the mass accretion and ejection processes, and non-thermal emission such as gyrosynchrotron radiation typically associated with Class II/III sources' (T-Tauri stars) intense magnetic activity. Our target is the young stellar cluster Ophiuchus A, a member of the Rho-Ophiuchi star-forming complex in the constellation Ophiuchus. This field is notable for its high population of YSOs at various evolutionary stages and for being one of the regions of its kind closest to the Solar System at approximately 139 pc (as estimated in [4]). In total, we have 17 different epochs spanning from 15/03/22 to 18/04/22 each with two slightly overlapping pointings, which adds up to 34 observations to analyse.

The main goals of this project are to first self-calibrate and process the VLA data in order to extract the real flux of the different YSOs in all the epochs, and then characterise their flux evolution in time so they can be classified into variable or non-variable sources. Finally, we try to infer the possible origins of the variability in some remarkable cases.

II. DATA PROCESSING

Unlike conventional optical telescopes, radio telescopes require a lattice of antennas in order to reach large enough collecting areas to pick up incoming radiation. Interferometry techniques combine all the signal into a unified interference pattern called visibility. Erratic fluctuations in phase and amplitude caused by meteorological conditions and bright sources located at the edges or even outside the primary beam create artifacts in the data that must be corrected.

For this purpose we used the Common Astronomy Software Applications (CASA; [5]) package, a post-processing program for radio telescope visibilities. The raw data was first calibrated with the VLA Calibration Pipeline within CASA (version 6.5.2), but self-calibration was applied afterwards to improve the quality of the final images. Self-calibration consists in correcting those artifacts by taking the bright sources in the field of view of the observation visibilities as a calibration model and thereby tailoring the correction to each source's specific properties, instead of using the phase calibrator data, which is usually shifted some degrees. We mainly employed the *tclean* and *gaincal* tasks: the former implements the CLEAN algorithm introduced by Högbgom in [6] with inverse Fourier transforms to generate the sky brightness distribution images from the interferometric patterns, while the latter builds the phase and amplitude correction tables for the data by comparing it to a

given calibration model.

The self-calibration process used in this project was designed with inspiration from the article in preparation [7] and CASA tutorials [8] and [9], and it works as follows. Firstly, an automatic mask is built only selecting pixels with a flux above $N \cdot$rms, being rms the root-mean-square background noise level. Keeping in mind that we had two different pointings for each epoch, as the second one had a very bright source, we had to set $N = 55$ to avoid including artifacts in the mask, whereas for the first pointing a value of $N = 20$ was high enough. Then, the calibration model is generated by a cleaning of the visibility guided by the mask using a Briggs robust weighting parameter of 0 and the results are used to compute the first phase correction tables. Next, the latter are applied to the visibility, which undergoes another masked cleaning and becomes the new model. This cyclic process is repeated iteratively until the signal-to-noise ratio (SNR) of the resulting image becomes approximately constant. In each iteration, the solution time interval for the phase correction is reduced from 220 s up to 2 s in multiples of 2, ensuring the final value is sufficiently short to exclude residual variations yet long enough to preserve the observation's intrinsic variability. Lastly, an amplitude correction is performed to minimize the remaining artifacts. Altogether, this self-calibration process has achieved average SNR improvements of 15 % for the first field and 80 % for the second, and has significantly reduced the original artifacts in the final images (see Appendix C).

To end up, a mosaic of the two pointings is built for each of the 17 epochs with the self-calibrated visibilities and yet a deeper masked cleaning process is done to obtain the resulting images. Aside from that, an additional mosaic is created by concatenating all the epochs into one single image. The latter has the highest sensitivity, therefore it is used to identify all the detected sources in the field and manually generate bounding boxes around them, which are then processed by the *imfit* task in CASA to extract properties such as position, flux or size by fitting a single elliptical Gaussian component.

III. RESULTS AND DISCUSSION

The resulting concatenated mosaic image has a beam of $0.343'' \times 0.181''$, a position angle of $-6.62°$ and a mean rms of 3.1 μJy beam^{-1}. A total of 22 sources have been detected above a $5 \cdot$ rms signal: 20 of them are YSOs (4 Class 0, 7 Class I, 6 Class II and 3 Class III) and the remaining 2 appear to be Galaxy Candidates. Moreover, among the 9 Class II/III YSOs, half of them (specifically: GSS29, GSS31a, GSS32 and GSS35) are catalogued as T-Tauri stars in the SIMBAD database and thus high variability is expected. For each of these sources, there has been obtained, along with their associated errors, the equatorial coordinates of the emission peak, the deconvolved size, the peak flux and the integrated flux in every epoch (see the summary table in Appendix A for the concatenated mosaic).

To evaluate the variability of their integrated flux we used the criterion of [10]. On the one hand, the difference between the maximum and minimum flux values (S_{diff}) shown by each source during the entire month of observations has been calculated, giving an idea of the maximum flux range achieved. On the other hand, the uncertainty of this value has been considered as $\sigma = \sqrt{\sigma_{\text{max}}^2 + \sigma_{\text{min}}^2}$, where σ_{max} and σ_{min} are, respectively, the uncertainties in the maximum and minimum flux values, and a flux threshold of $S_{\text{cutoff}} = 3\sigma$ has been established. Then, all sources with a flux variation of S_{diff} greater than this S_{cutoff} have been considered as variable, as this filters out any variability that might simply arise from measurement imprecisions. In this regard, it should be noted that the integrated flux for each source has been extracted by only a single Gaussian fit, meaning the flux values may have a non-negligible error, especially for fainter sources where, in some epochs, their signal was very close to the rms and even blended with it. To ensure some kind of reliability in this binary classification, sources with a flux difference between $3\sigma < S_{\text{diff}} < 5\sigma$ have been assigned a questionable variability, while those with $S_{\text{diff}} > 5\sigma$ have been classified as definitively variable.

Using this classification criterion, 15 out of the 22 sources have ultimately been considered as variable, 7 of them at the 3σ level and 8 at the 5σ. Table I shows the maximum and minimum flux values for each source, along with the corresponding cut-off flux and their classification as variable or non-variable. For the former, a variability percentage has also been included, calculated as $\% = (S_{\text{max}} - S_{\text{min}})/\langle S \rangle$, which gives an idea of the magnitude of the observed variation episodes relative to their average behaviour.

Given the limited extension of this project, among all the variable and non-variable sources detected, we have only selected a few notable cases to be analysed. The plots of their temporal flux curves can be seen in FIG. 1, altogether with a discontinuous line marking the cut-off threshold of 3σ (all the plots are shown in Appendix B). Firstly, we considered worth highlighting the results of GSS29 (see Appendix D) and GSS30-IRS2, where the flux spikes drastically one order of magnitude in just 5 to 10 days and remains nearly constant in the rest. This intense, short-timescale variability combined with the fact that both sources belong to Class II would be compatible with gyrosynchrotron emission produced by instabilities in their magnetospheres (as considered in [1] for another very young cluster in Corona Australis). In fact, an analysis of GSS29 in [11] with spectral indices between 7.5 and 10 GHz hints a large contribution of non-thermal emission in that source. However, polarization studies and observations at other frequencies (such as X-rays) would be needed to confirm this possible origin, given that emission in strong magnetic fields tends to be circularly polarized.

Another remarkable case is GSS23, where there appears to be a periodic oscillation trend with a timescale

TABLE I: Variability of all the detected radio sources at X-band.

Source Name	$S_{\max}$ (μJy)	$S_{\min}$ (μJy)	S_{diff} (μJy)	S_{cutoff} (μJy)	% Difference	Variable
VLA1623Aa	358.6 ± 100.5	131.9 ± 17.0	226.7 ± 101.9	305.8	—	N
VLA1623Ab	352.7 ± 22.3	60.2 ± 8.4	292.5 ± 23.8	71.5	143 ± 18	Y
VLA1623B	329.6 ± 37.9	173.0 ± 23.6	156.6 ± 44.6	133.9	62 ± 18	Y?
VLA1623W	197.9 ± 25.8	116.7 ± 29.6	81.2 ± 39.3	117.8	—	N
CRBR12	105.2 ± 14.4	28.2 ± 9.8	77.0 ± 17.4	52.3	106 ± 25	Y?
CRBR36	106.1 ± 30.9	32.4 ± 11.4	73.7 ± 32.9	98.8	—	N
CRBR2314.4-1237	577.2 ± 25.1	25.8 ± 14.5	551.4 ± 28.9	86.9	464 ± 146	Y
GSS23	104.6 ± 68.5	157.1 ± 26.0	888.5 ± 73.3	219.8	155 ± 22	Y
GSS26	127.9 ± 22.5	48.4 ± 14.2	79.5 ± 26.6	79.8	—	N
GSS29	1418.3 ± 24.7	35.5 ± 11.5	1382.8 ± 27.2	81.7	665 ± 271	Y
GSS30-IRS1	100.5 ± 13.9	52.9 ± 12.2	47.6 ± 18.5	55.5	—	N
GSS30-IRS2	5114.4 ± 68.4	204.0 ± 22.0	4910.4 ± 71.9	215.6	519 ± 180	Y
GSS30-IRS3	293.8 ± 26.6	229.9 ± 17.3	63.9 ± 31.7	95.2	—	N
GSS31a	116.7 ± 13.1	45.7 ± 11.3	71.0 ± 17.3	51.9	87 ± 22	Y?
GSS31b	96.6 ± 26.7	14.1 ± 4.9	82.5 ± 27.1	81.4	154 ± 54	Y?
GSS32	104.1 ± 18.0	25.3 ± 12.2	78.8 ± 21.7	65.2	108 ± 31	Y?
GSS35	6193.5 ± 91.6	3651.2 ± 114.0	2542.3 ± 146.2	438.7	51 ± 3	Y
LFAM3	205.2 ± 56.6	50.9 ± 13.7	154.3 ± 58.2	174.7	—	N
LFAM7	362.8 ± 76.4	39.1 ± 25.2	323.7 ± 80.4	241.3	252 ± 74	Y?
LFAM9	696.1 ± 39.2	18.1 ± 8.7	678.0 ± 40.5	120.5	520 ± 201	Y
LFAM13	211.8 ± 19.8	98.7 ± 10.2	113.1 ± 22.3	66.8	73 ± 15	Y
J162627.8-242359	111.6 ± 13.5	44.0 ± 12.2	67.6 ± 18.2	54.6	89 ± 24	Y?

Note. The columns show, in this order: Source Name: catalogue name of each source; $S_{\max}$ and $S_{\min}$: maximum and minimum integrated fluxes in X-Band in μJy; S_{diff}: difference between maximum and minimum fluxes in μJy; S_{cutoff}: 3σ threshold at which S_{diff} is considered as variability, in μJy; % Difference: percentage ratio between S_{diff} and the mean flux value; and Variable: variability classification. N means non-variable, Y? variable to the 3σ level and Y variable to the 5σ level.

longer than the resolution set by the span of our 1 month observation. In the SIMBAD catalogue, this source is classified as an Orion Variable (Haro 1-6) and it is an intermediate-mass pre-main sequence star called Herbig star. This would explain its variability, but in this case, a longer observation period would be needed to confirm whether these flux variations follow a periodic pattern or are merely coincidental.

Two other interesting cases are CRBR2314.4–1237 and LFAM9, as they belong to completely different classes yet exhibit locally similar flux curves. The former is a more evolved Class III YSO, while LFAM9 belongs to Class I still embedded in its dust and gas envelope. Given that the flux peak appears only in the last observed epoch, we cannot determine whether this might simply be a magnetospheric episode similar to those discussed for GSS29 and GSS30-IRS2 or whether it could instead be thermal free-free emission linked to a sudden matter ejection in the form of an outburst. For the latter hypothesis, it would be useful to have the full peak to compare the subsequent flux decay with the results of simulations of matter ejection under similar conditions for a better assumption.

Lastly, there is the Class 0 VLA1623A binary system, as it has also been addressed in [12] using the same raw data and variability criteria as this study. In their recent work, only 2 epochs were analysed and both sources, VLA1623Aa and VLA1623Ab, were treated as unresolved in the X-band due to the use of a Briggs robust weighting of 2 (i.e. natural) to produce the images, which prioritises sensitivity. Consequently, the system was considered as a single source with no variability at the 3σ level based on combined flux measurements and spectral index analysis across Q- (44 GHz), K- (22 GHz) and X-bands (10 GHz). In contrast, our treatment employs a robust weighting of 0, which better reveals the detail and has led to both components being marginally resolved. By manually defining separate regions for each source, we have been able to extract their respective fluxes. The resulting variability classification shows that while VLA1623Aa is clearly non-variable, its companion has a noticeably fast variability at the 5σ level. The previous non-variable classification of the system could thus be explained by the flux dominance of VLA1623Aa, which in [12] they found to be approximately twice as bright as VLA1623Ab.

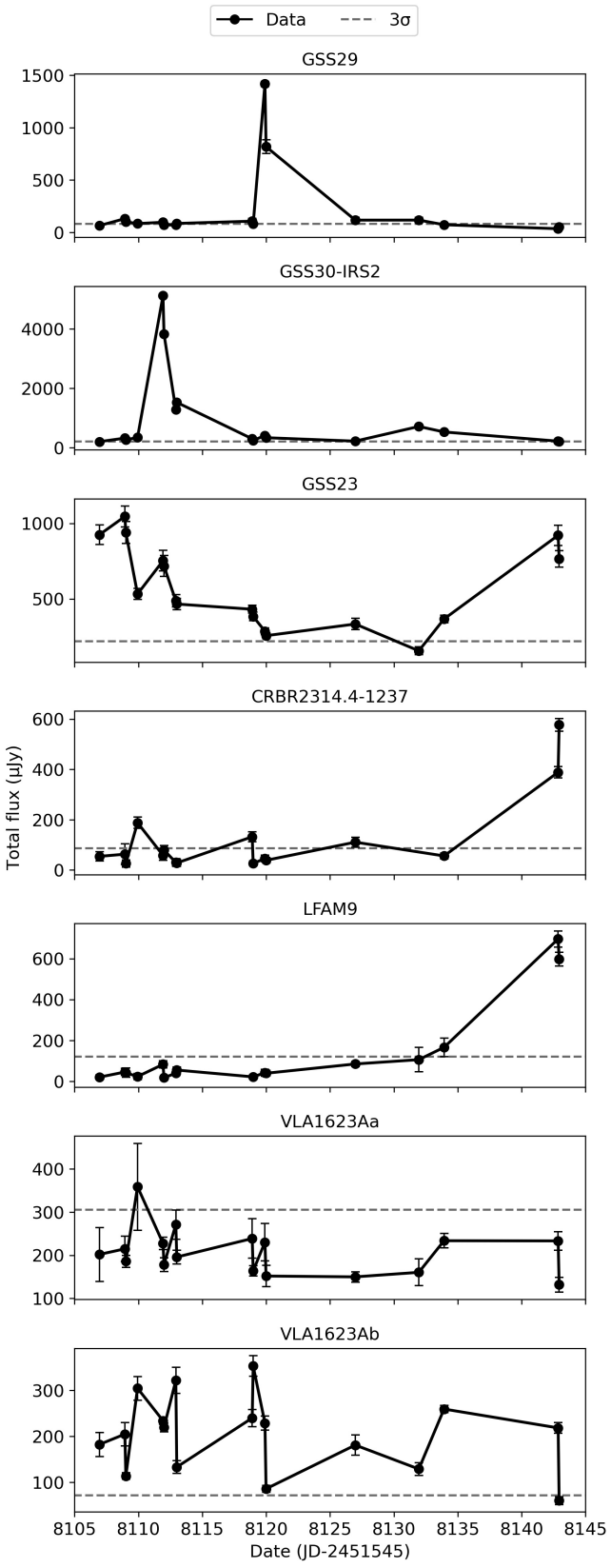

FIG. 1: Flux curves of GSS29, GSS30-IRS2, GSS23, CRBR2314.4–1237, LFAM9, VLA1623Aa and VLA1623Ab; from top to bottom in this order. A dashed horizontal line shows the 3σ level in each case.

As a summary of the results, FIG. 2 displays the histogram comparing S_{diff} to S_{cutoff} values for each of the detected sources, grouped by evolutionary stage. It should be noticed that the flux axis uses a logarithmic scale to prevent highly variable sources such as GSS29 or GSS30-IRS2 from dominating the visualization. Also, it can be clearly seen that the amount of variable YSOs with large flux differences increases as they belong to more evolved classes (Class II/III), with the notable exception of the Class 0 VLA1623Ab mentioned earlier. While a larger sample size would be needed in order to claim such trend, our results appear consistent with the framework proposed in [1]. That is, the emission from Class 0/I sources would be less variable as they are surrounded by an optically thick envelope of gas and dust that attenuates most of it whereas in Class II/III sources most of the material resides primarily in the disc, thus leaving their active magnetosphere responsible of non-thermal emissions more exposed.

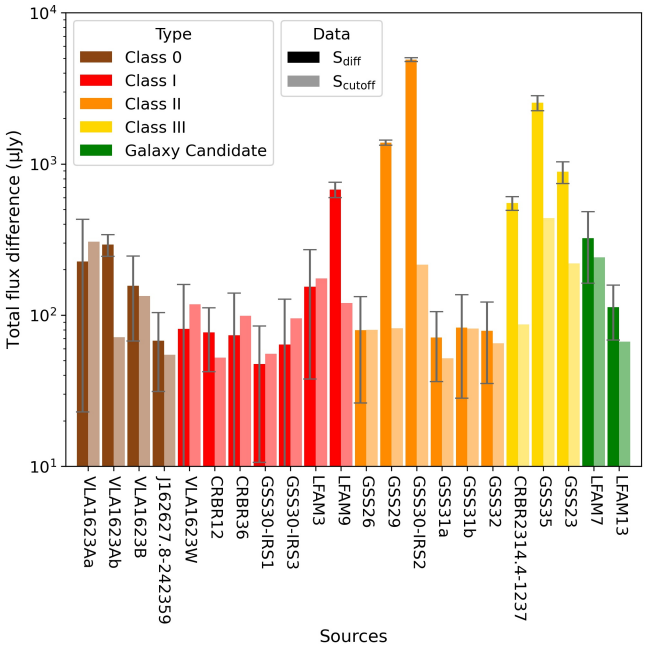

FIG. 2: Histogram of all YSOs detected in X-band grouped by evolutionary stage comparing S_{diff} (opaque bars) with S_{cutoff} (washed bars) in logarithmic scale. Both Galaxy Candidates are also present in green. Error bars in S_{diff} show a 2σ margin to distinguish 3σ variable sources from 5σ.

IV. CONCLUSIONS

In this project, we have successfully applied self-calibration techniques to the initial VLA X-band data, ultimately producing a series of mosaic images for 17 different observation epochs spanning over one month. This process has led to a significant improvement in data quality, with the average SNR increasing from 209 to 351, rep-

resenting a 68 % enhancement. Through careful analysis of these mosaics, we have identified a total of 22 sources, comprising 20 YSOs belonging to all sort of evolutionary stages and 2 Galaxy Candidates. Among these, our analysis has classified 15 objects as exhibiting variable behaviour, with half of these variable sources showing variability at a confidence level exceeding 5σ (i.e. up to a 99.977 % certainty).

By constructing flux curves for all these sources, we have been able to conduct a preliminary investigation of several particularly interesting cases, though we emphasize that these interpretations remain hypothetical without further supporting evidence. Notable examples include the discrete flux spikes observed in GSS29 and GSS30-IRS2 (both Class II sources), CRBR2314.4-1237 (a Class III source), and LFAM9 (a Class I source). We have also highlighted the potential periodicity in the Orion Variable GSS23 and the variable emission in the young binary system VLA1623A. However, we have not been able to reach to solid conclusions, as establishing firmer explanations would require more detailed, source-specific analyses that exceed the scope of this work.

In fact, a direct continuation of this study would involve calculating the structure function for each of the identified variable sources to estimate their characteristic variability timescale. This analytical approach, as described in [1], involves dividing the total observation period into discrete time intervals $t_{ij} = t_i - t_j$ and computing the flux differences for each interval, weighted by the overall flux standard deviation ($F_{ij} = (S_i - S_j)^2/\sigma^2$). Plotting these values against their respective time intervals would reveal the dominant variability timescale through the position of the maximum in the resulting function.

Moreover, in order to achieve more robust identification of the observed variability phenomena, it would be interesting to match our observations with their counterparts in other wavelengths. For example, correlating our X-band data with X-ray observations could allow us to test the Güdel-Benz relation (as done in [10]), potentially distinguishing between thermal and non-thermal emission mechanisms. Otherwise, a spectral index analysis with observations of the same region in other frequencies (K-, Q-band and data from ALMA archive) could further constrain the thermal nature of the emission processes. In addition, with access to polarization data and a longer temporal coverage, we could identify whether the variability in GSS23 is actually periodic and better characterize the thermal versus non-thermal origins of the flux variations observed in CRBR2314.4-1237 and LFAM9.

Finally, the launching of next-generation radio interferometers such as the Square Kilometre Array (SKA) and the Next Generation Very Large Array (ngVLA), promises to revolutionize this field of study. These advanced instruments will offer unprecedented capabilities, including faster sky surveys with higher temporal resolution, improved sensitivity and angular resolution, and broader frequency coverage. Such technological advancements will undoubtedly provide the tools necessary to address questions still unresolved on this research field.

Acknowledgments

I would like to express my most sincere gratitude to my advisor Dra. Gemma Busquet for her invaluable guidance and unwavering support throughout this project. Her expertise and encouragement were crucial in overcoming the numerous challenges encountered during this study. I am also profoundly grateful to Dr. Álvaro Sánchez-Monge and Elena Díaz-Márquez for their contributions during the final stages of this work.

[1] H. B. Liu et al. "Time monitoring of radio jets and magnetospheres in the nearby young stellar cluster R Coronae Australis". The Astrophysical Journal **780**, 115 (2014)

[2] W. J. Fischer et al. "Accretion variability as a guide to stellar mass assembly". Protostars and Planets VII (2023)

[3] G. Busquet et al. "Grain growth in protoplanetary disks in Ophiuchus A cluster". Observing Application VLA/22A-164 (2021)

[4] C. Zucker et al. "A compendium of distances to molecular clouds in the star formation handbook". Astronomy & Astrophysics **633**, A51 (2020)

[5] "Common Astronomy Software Applications (CASA)". `https://casa.nrao.edu/`

[6] J. A. Högbom "Aperture synthesis with a non-regular distribution of interferometer baselines". Astronomy and Astrophysics Supplement **15**, 417 (1974)

[7] E. Díaz-Márquez et al. "The VLA Orion A Large Survey (VOLS). II. Data processing and imaging at C-band". Astronomy & Astrophysics (in preparation)

[8] "VLA self-calibration tutorial CASA 5.7.0". `https://casaguides.nrao.edu/index.php/VLA_Self-calibration_Tutorial-CASA5.7.0`

[9] "First look at self-calibration CASA 6.5.4". `https://casaguides.nrao.edu/index.php/First_Look_at_Self_Calibration_CASA_6.5.4`

[10] E. Díaz-Márquez et al. "Radio survey of the stellar population in the infrared dark cloud G14.225-0.506". Astronomy & Astrophysics **682**, A180 (2024)

[11] A. Coutens et al. "VLAcm-wave survey of young stellar objects in the Oph A cluster: constraining extreme UV- and X-ray-driven disk photoevaporation. A pathfinder for Square Kilometre Array studies". Astronomy & Astrophysics **631**, A58 (2019)

[12] I. C. Radley et al. "Characterising the multiple protostellar system VLA 1623–2417 with JWST, ALMA and VLA: outflow origins, dust growth and an unsettled disk". The Astrophysical Journal **981**, 187 (2025)

Variabilitat ràdio en el cúmul estel·lar jove Ophiuchus A

Author: Arnau Vicente Bou, avicenbo74@alumnes.ub.edu
Facultat de Física, Universitat de Barcelona, Diagonal 645, 08028 Barcelona, Spain.

Advisor: Gemma Busquet Rico, gbusquet@fqa.ub.edu

Resum: Mitjançant dades de la banda X (10 GHz) del VLA obtingudes durant l'observació del cúmul estel·lar jove Ophiuchus A, hem estudiat la variabilitat de flux de les fonts en aquesta regió al llarg de 17 èpoques diferents en un període d'aproximadament un mes. En la primera part d'aquest treball, hem aplicat un procés iteratiu d'autocalibració a les visibilitats per corregir errors de fase i amplitud, tot generant un mosaic de dos camps per cada època. En la segona part, hem extret els fluxos de les 22 fonts detectades en totes les èpoques i les hem classificat com a variables o no variables seguint un criteri que compara la diferència màxima de flux de cada font amb un llindar que té en compte tant el rms com les incerteses de la calibració. Els resultats mostren evidència de variabilitat en 15 de les 22 fonts detectades, i analitzem alguns casos destacats com els pics abruptes de flux observats en GSS29 i GSS30-IRS2 o l'emissió variable del sistema binari VLA1623A. A més, el comportament de la mostra estudiada sembla concordar amb el consens general que la variabilitat dels objectes estel·lars joves (YSOs) augmenta en etapes evolutives més avançades.
Paraules clau: formació estel·lar, núvol molecular, disc d'acreció, emissió tèrmica, variabilitat de flux.
ODSs: Aquest TFG està relacionat amb els Objectius de Desenvolupament Sostenible (SDGs).

Objectius de Desenvolupament Sostenible (ODSs o SDGs)

1. Fi de les desigualtats		10. Reducció de les desigualtats	
2. Fam zero		11. Ciutats i comunitats sostenibles	
3. Salut i benestar		12. Consum i producció responsables	
4. Educació de qualitat	X	13. Acció climàtica	
5. Igualtat de gènere		14. Vida submarina	
6. Aigua neta i sanejament		15. Vida terrestre	
7. Energia neta i sostenible		16. Pau, justícia i institucions sòlides	
8. Treball digne i creixement econòmic		17. Aliança pels objectius	X
9. Indústria, innovació, infraestructures	X		

El contingut d'aquest treball està relacionat amb l'ODS 4, perquè proporciona informació a nivell tècnic contrastada entre diverses fonts. També va lligat a l'ODS 9, ja que al final es fa referència als avantatges que aportaran els radio interferòmetres del futur. Per últim, aquest treball es pot associar a l'ODS 17, en tant que forma part d'un projecte més gran en què hi col·labroren investigadors de moltes disciplines diferents.

GRAPHICAL ABSTRACT

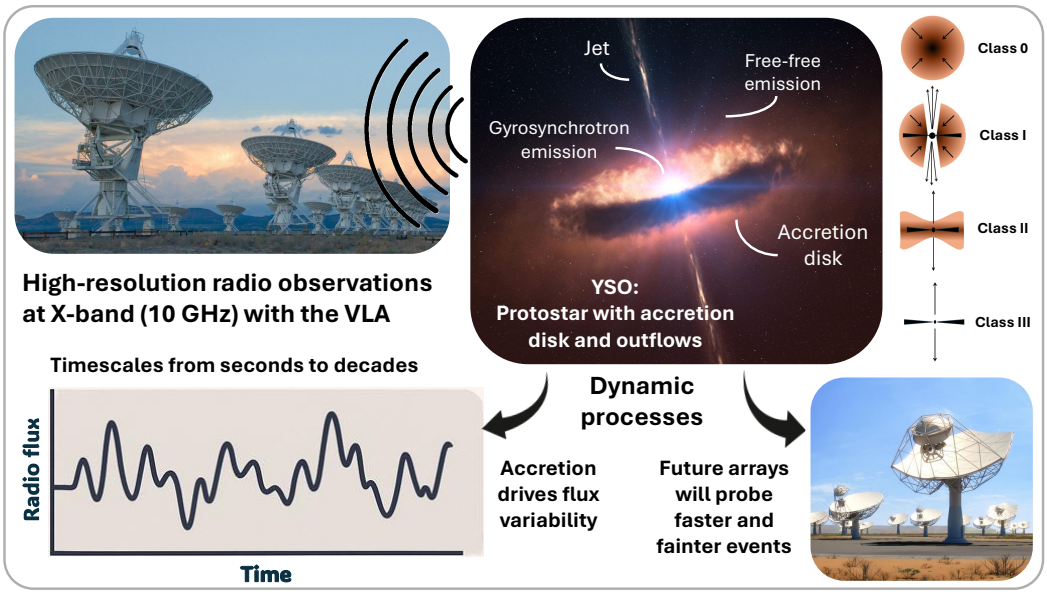

Appendix A: Detected sources in the concatenated mosaic

TABLE II: Global data table of the sources detected in the concatenated mosaic image.

Source Name	R.A. (J2000)	Dec. (J2000)	Deconvolved Size (marcsec)	P.A. (deg.)	$S_{\rm peak}$ (μJy/beam)	$S_{\rm int}$ (μJy)	Classification
VLA1623Aa	16:26:26.3942	-24:24:30.9507	$249 \times 169 \pm (37 \times 76)$	108 ± 32	113.9 ± 5.6	212.0 ± 15.0	Class 0
VLA1623Ab	16:26:26.3889	-24:24:30.9614	$422 \times 157 \pm (48 \times 104)$	90 ± 13	98.7 ± 7.4	274 ± 27	Class 0
VLA1623B	16:26:26.3038	-24:24:30.8166	$179 \times 92 \pm (26 \times 57)$	76 ± 33	184.1 ± 8.3	267 ± 19	Class 0
J162627.8-242359	16:26:27.8506	-24:23:59.7088	Point Source	—	63.8 ± 3.0	76.0 ± 6.0	Class 0
VLA1623W	16:26:25.6281	-24:24:29.7069	$178 \times 119 \pm (24 \times 94)$	93 ± 54	103.0 ± 4.1	152.7 ± 9.4	Class I
CRBR12	16:26:17.2299	-24:23:45.8878	Point Source	—	61.3 ± 2.1	70.7 ± 4.1	Class I
CRBR36	16:26:25.4724	-24:23:01.9359	Point Source	—	40.8 ± 3.1	37.3 ± 5.5	Class I
GSS30-IRS1	16:26:21.3554	-24:23:05.0053	Point Source	—	74.0 ± 3.0	69.4 ± 5.4	Class I
GSS30-IRS3	16:26:21.7163	-24:22:51.0759	$195 \times 52 \pm (20 \times 43)$	33 ± 8	210.0 ± 4.2	277.3 ± 9.1	Class I
LFAM3	16:26:23.5728	-24:24:40.1150	$173 \times 81 \pm (39 \times 57)$	124 ± 25	73.8 ± 3.2	99.1 ± 6.9	Class I
LFAM9	16:26:30.5337	-24:22:57.3774	$108 \times 103 \pm (44 \times 80)$	177 ± 83	110.0 ± 3.5	132.7 ± 7.2	Class I
GSS26	16:26:10.3260	-24:20:55.3754	$205 \times 93 \pm (27 \times 81)$	52 ± 16	53.5 ± 1.8	80.1 ± 4.3	Class II
GSS29	16:26:16.8451	-24:22:23.7382	Point Source	—	227.7 ± 5.7	204.6 ± 9.8	Class II
GSS30-IRS2	16:26:22.3859	-24:22:53.5634	Point Source	—	911.0 ± 12.0	922 ± 23	Class II
GSS31a	16:26:23.3592	-24:21:00.1013	Point Source	—	82.1 ± 2.6	80.1 ± 4.8	Class II
GSS31b	16:26:23.4275	-24:21:01.8597	Point Source	—	34.8 ± 1.5	36.3 ± 2.8	Class II
GSS32	16:26:24.0381	-24:24:48.6362	$141 \times 69 \pm (45 \times 30)$	25 ± 35	52.3 ± 1.8	62.5 ± 3.7	Class II
CRBR2314.4-1237	16:26:15.8148	-24:19:22.6085	$107 \times 71 \pm (44 \times 47)$	160 ± 88	100.4 ± 2.7	113.3 ± 5.3	Class III
GSS23	16:26:02.9936	-24:23:36.6291	$142 \times 75 \pm (30 \times 57)$	108 ± 43	432.0 ± 15.0	552 ± 32	Class III
GSS35	16:26:34.1717	-24:23:28.8122	Point Source	—	4546.0 ± 47.0	4809 ± 90	Class III
LFAM7	16:26:29.6141	-24:23:17.2337	$751 \times 81 \pm (149 \times 129)$	83 ± 6	22.6 ± 3.6	99 ± 19	Galaxy Candidate
LFAM13	16:26:35.3299	-24:24:05.2922	$118 \times 47 \pm (49 \times 40)$	139 ± 26	146.6 ± 5.8	166 ± 11	Galaxy Candidate

Note. The columns show, in this order: Source Name: catalogue name of each source; R.A.: right ascension (in hh:mm:ss); Dec.: declination (in $^{\rm o}$:':"); Deconvolved Size: image component size of the source deconvolved from beam in marcsec (in format Maj. axis X Min. axis); P.A.: position angle in degrees; $S_{\rm peak}$: peak flux in μJy beam^{-1}; $S_{\rm int}$: integrated flux in μJy; and Classification: YSO evolutionary state (excepting the two Galaxy Candidates).

Appendix B: Flux curves

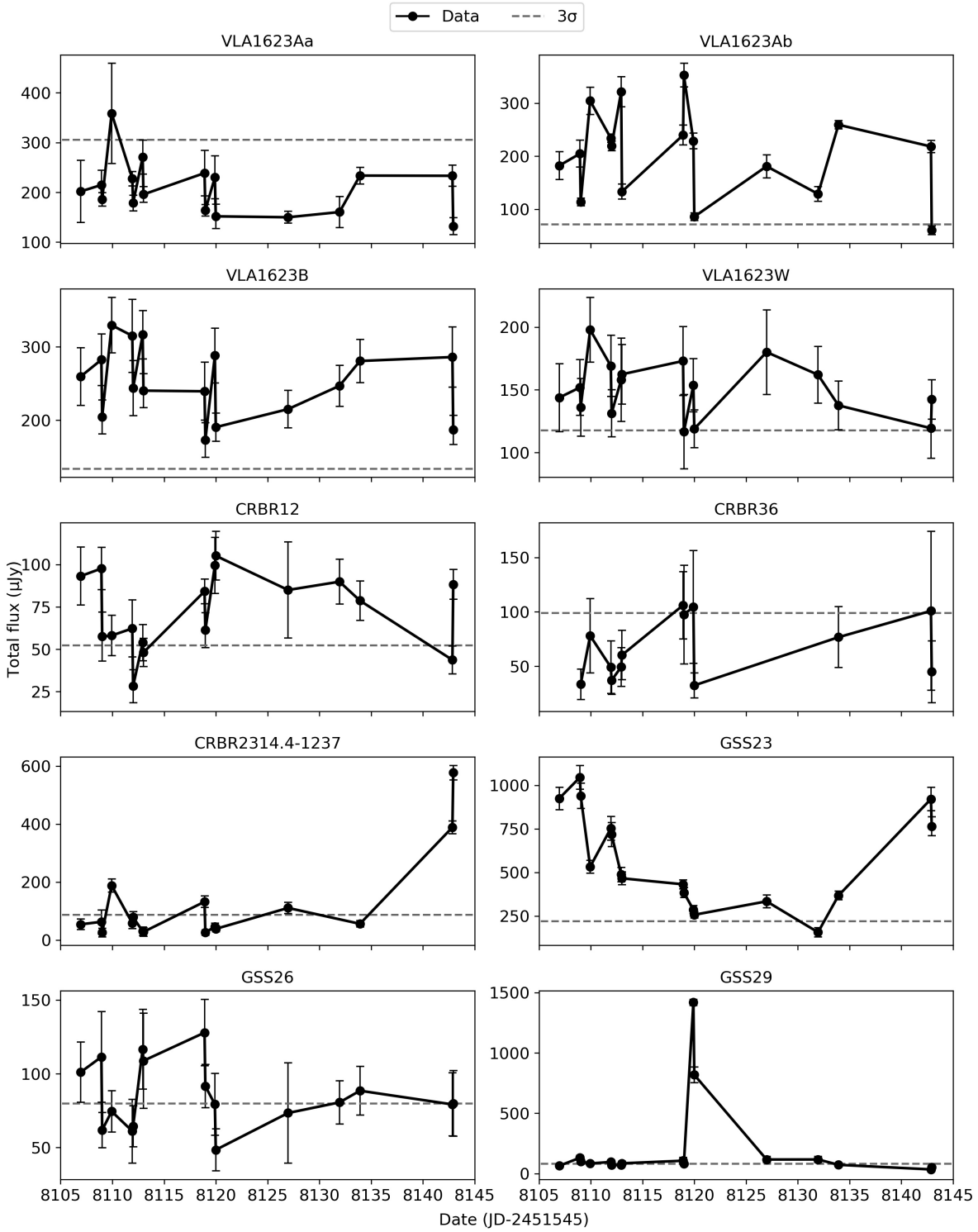

FIG. 3: Flux curves of all sources detected. The name of the source is above each of the plots, and a dashed horizontal line shows the 3σ level in each case.

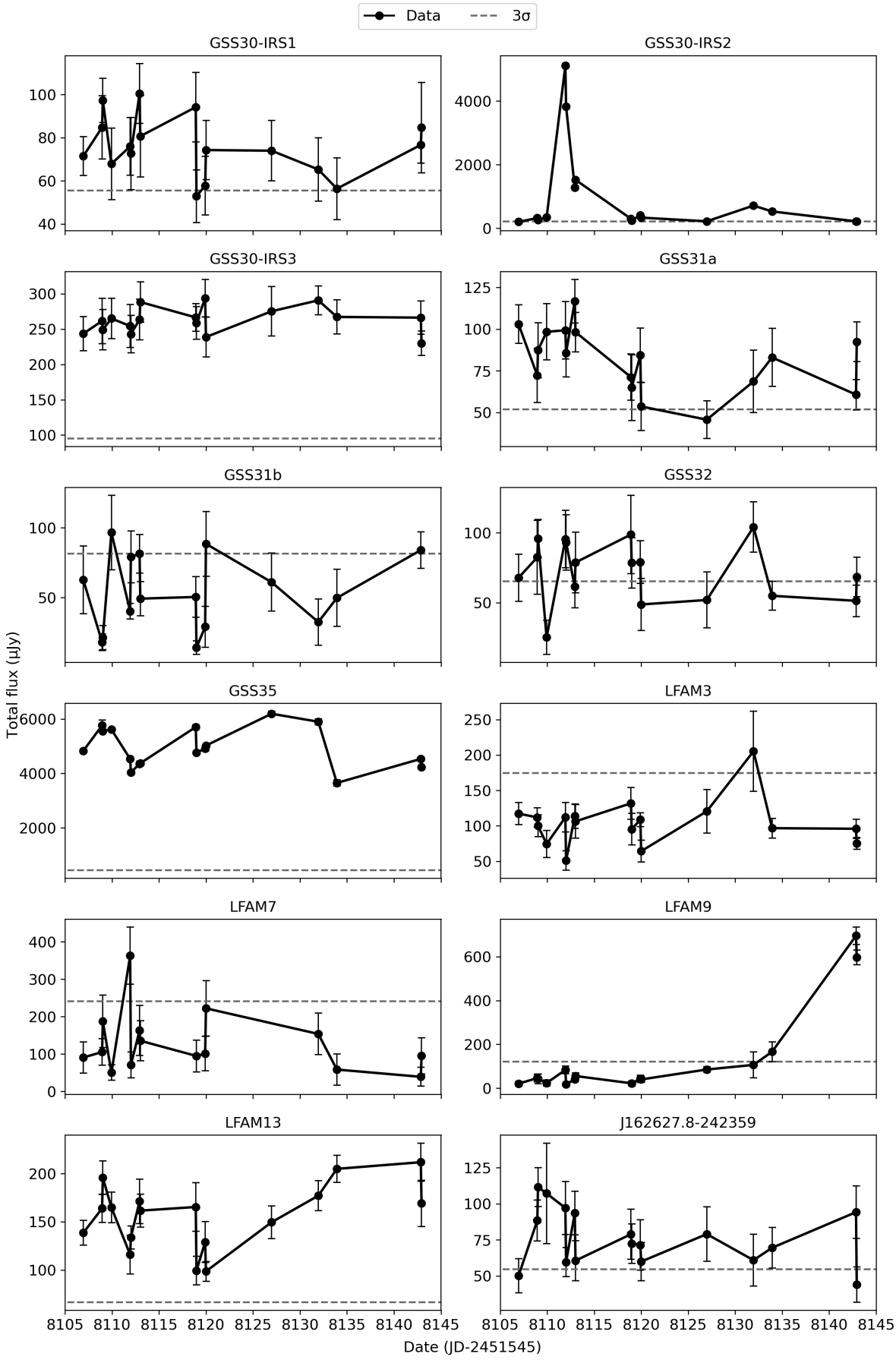

FIG. 4: Same as FIG.3.

Appendix C: Self-calibration results

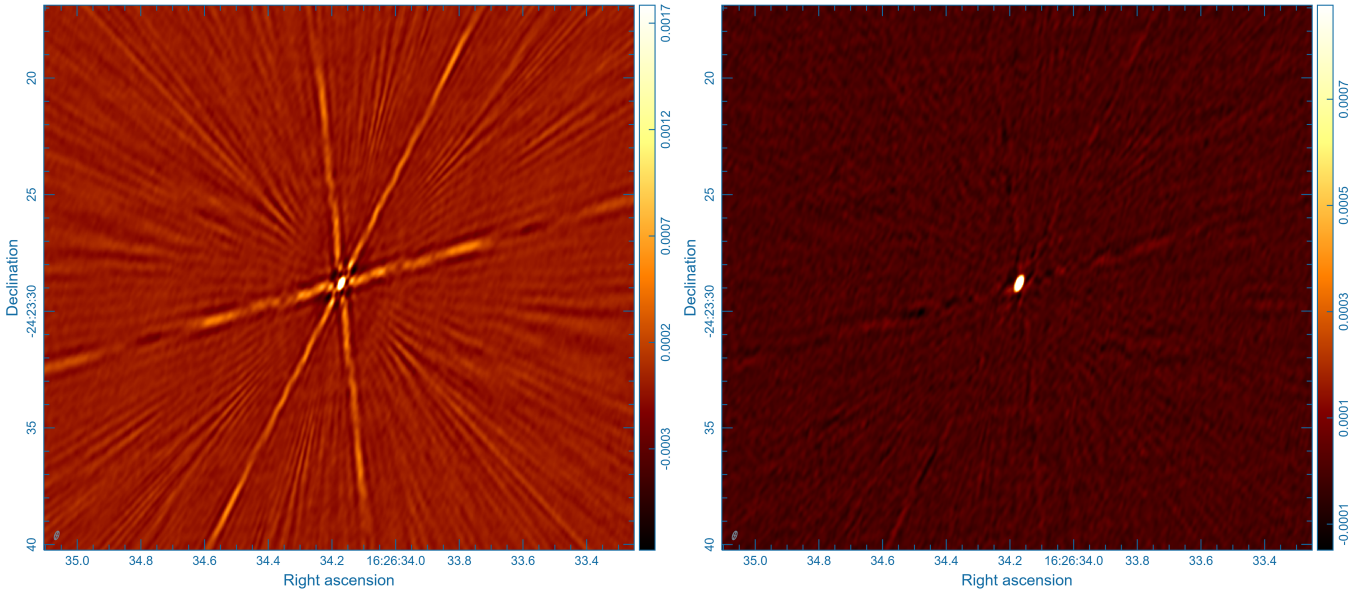

FIG. 5: Comparison between the dirty (to the left) and the self-calibrated (to the right) clean mosaic image of the brightest source in the field, GSS35. The colour pallet shows flux values in Jy beam^{-1}. This figure has been generated with CARTA image visualization and analysing tool.

Appendix D: Emission variability images

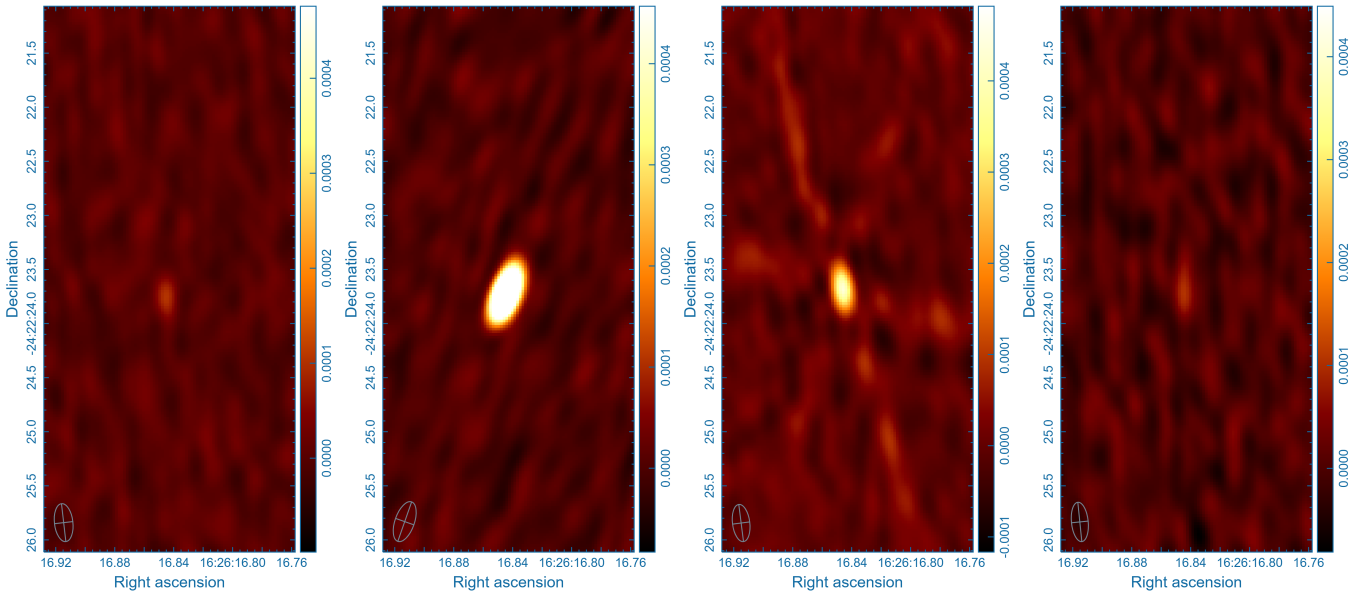

FIG. 6: Evolution, from left to right, of the radio emission in GSS29 around the peak measured among 10th and 12th epoch. The colour pallet shows flux values in Jy beam^{-1}. This figure was also generated with CARTA.